

# Genesis and trends in marine heatwaves over the tropical Indian Ocean and their interaction with the Indian summer monsoon

**J. S. Saranya<sup>1,2</sup>, M K Roxy<sup>1\*</sup>, Panini Dasgupta<sup>1,3</sup> and Ajay Anand<sup>1,4</sup>**

<sup>1</sup> *Centre for Climate Change Research, Indian Institute of Tropical Meteorology, Pune 411008, India*

<sup>2</sup> *College of Climate Change and Environmental Sciences, Kerala Agricultural University, Kerala, 680656, India*

<sup>3</sup> *Department of Meteorology and Oceanography, College of Science and Technology, Andhra University, Visakhapatnam, Andhra Pradesh 530003, India*

<sup>4</sup> *Department of Atmospheric Sciences, Cochin University of Science and Technology, Kerala, 682022, India*

## Key points:

- An increasing trend in marine heatwaves is observed over the western Indian Ocean and the Bay of Bengal.
- Ocean warming and El Niño events drives the genesis and trends of marine heatwaves in the Indian Ocean.
- Marine heatwaves reduce the monsoon rainfall over the central Indian subcontinent while enhancing it over the southern peninsula.

*JGR Oceans*, submitted on 31 March 2021, Revised on 3 July 2021

---

\*Corresponding author address: Roxy Mathew Koll, Indian Institute of Tropical Meteorology, Pune 411008, India. E-mail: roxy@tropmet.res.in

## 24    **Abstract**

25    Marine heatwaves (MHWs) are extreme oceanic warm water events (above 90<sup>th</sup> percentile threshold)  
26    that significantly impact the marine environment. Several studies have recently explored the genesis  
27    and impacts of MHWs though they are least understood in the tropical Indian Ocean. Here we  
28    investigate the genesis and trend of MHWs in the Indian Ocean during 1982–2018 and their role in  
29    modulating the Indian monsoon. We find that the rapid warming in the Indian Ocean plays a critical  
30    role in increasing the number of MHWs. Meanwhile, the El Niño has a prominent influence on the  
31    occurrence of MHWs during the summer monsoon. The Indian Ocean warming and the El Niño  
32    variability have synergistically resulted in some of the strongest and long-lasting MHWs in the  
33    Indian Ocean.

34        The western Indian Ocean (WIO) region experienced the largest increase in MHWs at a rate of  
35    1.2–1.5 events per decade, followed by the north Bay of Bengal at a rate of 0.4–0.5 events per  
36    decade. Locally, the MHWs are induced by increased solar radiation, relaxation of winds, and  
37    reduced evaporative cooling. In the western Indian Ocean, the decreased winds further restrict the  
38    heat transport by ocean currents from the near-equatorial regions towards the north. Our analysis  
39    indicates that the MHWs in the western Indian Ocean and the north Bay of Bengal lead to a  
40    reduction in monsoon rainfall over the central Indian subcontinent. On the other hand, there is an  
41    enhancement of monsoon rainfall over southwest India due to the MHWs in the Bay of Bengal.

42

## 43    **Plain Language Summary**

44    Marine heatwaves are periods of extremely high temperatures in the ocean. Though several studies  
45    have reported their occurrence and impacts in the global oceans, they are least understood in the  
46    tropical Indian Ocean. In the current study, we find that marine heatwaves are increasing in the  
47    Indian Ocean, with the largest increase observed over the western Indian Ocean, followed by the  
48    north Bay of Bengal. These marine heatwaves occur as a result of background ocean warming in the

Indian Ocean and also in response to El Niño events in the Pacific Ocean. Locally, a peak in solar radiation and a dip in evaporative cooling due to weak winds lead to the formation of these marine heatwaves. In the western Indian Ocean, the weak winds also reduce the heat transported by ocean currents from the near-equatorial regions towards the north, intensifying the marine heatwave. In turn, these marine heatwaves impact the monsoon by reducing the rainfall over the central Indian subcontinent while enhancing it over the southern peninsula.

55

## 56 **1. Introduction**

According to the Special Report on the Ocean and Cryosphere (SROCC) of the Intergovernmental Panel on Climate Change (IPCC), the global ocean will continue to warm during the 21<sup>st</sup> century (IPCC, 2019). By 2100, the ocean warming in the top 2000 m is estimated to be 5–7 times higher under the business-as-usual scenario and 2–4 times higher under the low emission scenario, relative to the temperature reported since 1970 (*very likely*). Under this warming scenario, a rise in extreme temperature events in the ocean is also projected. Marine heatwaves (MHWs) are anomalous warm water events a response to the warming ocean—defined when the daily sea surface temperature (SST) exceeds the 90<sup>th</sup> percentile for five or more days (percentile threshold may vary and can be as high as the 99<sup>th</sup> percentile) (Hobday et al., 2016, Schaeffer et al., 2017, Collins et al., 2019). MHWs are reported all over the world—the 2003 Mediterranean Sea MHW, 2011 West Australian MHW, 2015/16 Tasman Sea MHW are some of them. Numerous studies indicate that these anomalous temperature events can cause habitat destruction due to coral bleaching, seagrass destruction, and loss of kelp forests, affecting the fisheries sector adversely (Mills et al., 2013, Collins et al., 2019).

Numerous studies have focused on the mechanisms leading to the genesis of MHWs. Most of the MHWs in Indo-Pacific regions are associated with climate modes like the El Niño, the Indian Ocean Dipole (IOD), and the Pacific Decadal Oscillation (PDO). The 2014–2015 MHW in the Northeast Pacific was associated with the PDO and the North Pacific Gyre Oscillation (NPGO).

74 These modes enhanced the conditions that led to an increase in SST in the Northeast Pacific (Joh and  
75 Lorenzo, 2017). Holbrook et al. (2019) had suggested that the SST variability in the tropical Indian  
76 and Pacific oceans is related to the El Niño, IOD, and Indian Ocean warming.

77 Although several studies have explored the extreme temperature events in the Pacific and  
78 Atlantic oceans, there is hardly any in-depth research on MHWs in the Indian Ocean. In the southeast  
79 Indian Ocean, coral bleaching events due to the MHWs were reported, mostly associated with the El  
80 Niño and Madden-Julian Oscillations (MJO), riding over a global warming signal (Zhang et al.,  
81 2017). Studies have reported high SST conditions in the western Indian Ocean (Seychelles region),  
82 Arabian Sea, and the Bay of Bengal region (Andaman Sea) and also point out the coral bleaching  
83 events due to intense warming in these regions (Saji et al., 1999; Edward et al., 2018; Raj et al.,  
84 2018; Krishnan et al., 2011).

85 The north Indian Ocean is a critical region because it supports large marine primary  
86 productivity, particularly during the South Asian summer monsoon (Roxy et al., 2016), and because  
87 of its role in modulating the intraseasonal and interannual variability of the monsoon (Roxy et al.,  
88 2007, 2012; Singh and Dasgupta 2017). Understanding the genesis and evolution of MHWs during  
89 the summer monsoon season and their changes due to ocean warming is hence crucial. In this study,  
90 for the first time, we explore the genesis and trend of MHWs in the Indian Ocean during the summer  
91 monsoon season (June–September). While many studies have addressed the impacts of MHWs on  
92 the marine ecosystem, there are hardly any studies investigating the impacts of MHWs on  
93 atmospheric circulation and rainfall. Hence, we investigate the interaction between MHWs and  
94 Indian summer monsoon circulation and rainfall.

95

## 96 **2. Data and methods**

### 97 **2.1 Data**

98 To identify the MHWs, we used the daily Optimum Interpolated Sea Surface Temperature (OISST)  
 99 dataset at a resolution of  $0.25^\circ \times 0.25^\circ$ , for the period 1982–2018 (Reynolds et al., 2007). In order to  
 100 study the impact of MHWs on atmospheric conditions, we used the daily NOAA Interpolated  
 101 Outgoing Longwave Radiation (OLR) measured from Advanced Very High-Resolution Radiometer  
 102 (AVHRR) onboard NOAA polar-orbiting spacecraft (Liebmann and Smith, 1996), at a  $2.5^\circ \times 2.5^\circ$   
 103 resolution, for the period 1982–2018. The daily wind, latent heat flux, sensible heat flux, upward  
 104 longwave radiation, downward solar radiation, surface net longwave radiation, and surface net solar  
 105 radiation are obtained from the National Center for Environmental Prediction/National Centers for  
 106 Atmospheric Research (NCEP/NCAR) reanalysis data at a resolution of  $2.5^\circ \times 2.5^\circ$  (Kalnay et al.,  
 107 1996). For the analysis of the rainfall variability over India, we used IMD daily rainfall at a  
 108 resolution of  $0.25^\circ \times 0.25^\circ$  (Pai et al., 2014). All the analyses are compared with European Centre for  
 109 Medium-Range Weather Forecasts (ECMWF) ERA5 reanalysis product (Hersbach and Dee, 2016).  
 110 In the main text, we use NCEP/NCAR products, and in the supplementary information, we compare  
 111 our results with ERA5 reanalysis products.

112 To investigate the ocean conditions during the MHWs, we obtained the ocean current data at  
 113  $1/3^\circ$  grid with a five-day temporal resolution from the Ocean Surface Current Analysis Real-time  
 114 (OSCAR) (Dohan and Maximenko, 2010). The monthly potential temperature and salinity are  
 115 obtained from ORAS4 at a horizontal resolution of  $1^\circ \times 1^\circ$  (Balmaseda et al., 2013). Apart from this,  
 116 daily water temperature and salinity are obtained from the Hybrid Coordinate Ocean Model  
 117 (HYCOM) reanalysis. We supplemented the heat budget analysis using the HYCOM reanalysis  
 118 (Metzger et al., 2014) at a resolution of  $1/12^\circ$  for 1994–2015.

119

## 120 **2.2 Methods**

### 121 **2.2.1 Detection of marine heatwaves**

122 In this study, we identify MHWs from the OISST daily datasets, where the SST is above the 90<sup>th</sup>  
123 percentile (threshold) and persist for at least five days. Here, the 90<sup>th</sup> percentile and the baseline  
124 climatology of SST are calculated for each calendar day from the daily SSTs using an 11-day  
125 window centered on that particular day of the year, across all years, within the climatology period  
126 (1982–2018)—and are smoothed using a 31-day moving average (Hobday et al. 2016, Oliver et al.  
127 2018, Sen Gupta et al. 2020). The reason for considering an 11-day window is to create enough  
128 sample size for the 90<sup>th</sup> percentile estimation at a daily timescale and also to eliminate the occasional  
129 outliers that might pop up with a shorter sample size. The 31-day moving average is used to obtain a  
130 smoothed climatology that is seasonally varying and does not contain any higher-frequency  
131 variability than the seasonal timescale (below 30 days). This seasonally varying 90<sup>th</sup> percentile will  
132 help us to identify the MHWs at any time of the year, regardless of the summer months (Oliver et al.,  
133 2018). We also utilize specific metrics to study and analyze the MHWs, such as the maximum  
134 intensity (maximum temperature anomaly during a particular MHW event), mean intensity (mean  
135 temperature anomaly during a specific MHW event), cumulative intensity (sum of temperature  
136 anomalies during a particular MHW event), duration (number of days between the starting and  
137 ending dates), and spatial extent (area covered by MHW event) (Hobday et al., 2016). To study the  
138 spatial extent of the MHWs, we counted the grids where the MHW events occurred and multiplied  
139 them by the grid area. To estimate the trend in MHWs, we used the OISST data from 1982–2018 and  
140 calculated MHW at each grid, and then fit a linear trend model. Along with the annual values, we  
141 also prepare the MHW metrics for June to September.

142 Further, we did a composite analysis of wind, SST, latent heat flux, sensible heat flux,  
143 upward longwave radiation, and downward solar radiation during one week before and after the  
144 starting date of MHW events. This provides us with a comprehensive picture of the genesis of  
145 MHWs and describes the physical and dynamical processes involved with the MHW genesis over the  
146 particular regions. To study the interaction between the MHWs and summer monsoon circulation and

rainfall, we have included a composite analysis of wind at 850 hPa, OLR, omega at 500 hPa, vertically integrated moisture flux, and rainfall over India during the MHWs.

### 2.2.2 Mixed layer heat budget

To study the local factors influencing the genesis of MHWs, we estimated the mixed layer heat budget using the temperature tendency equation. The temperature tendency equation gives us a comprehensive picture of factors that lead to the change in the ocean surface temperature (Rodrigues et al., 2019). The temperature tendency equation is given by

$$\partial T_m / \partial t = -v \cdot \nabla T + Q_0 / \rho C_p H_m + Res \quad (1)$$

where  $\rho$  is the density of seawater ( $1,026 \text{ kg m}^{-3}$ ), and  $C_p$  is the specific heat of seawater ( $3902 \text{ J kg}^{-1} \text{ K}^{-1}$ ), and  $T_m$  is the mixed layer temperature. Here we have used the SST as a mixed layer temperature because the vertically averaged mixed layer temperature is close to the SST values (Foltz et al., 2003).

$\partial T_m / \partial t$  represents the rate of change of mixed layer temperature. The term  $-v \cdot \nabla T$  indicates the advection and  $v$  indicate the horizontal velocity vector ( $v$  at 15m depth from OSCAR Ocean currents, vertically averaged over the mixed layer).  $H_m$  means the mixed layer depth (MLD) in meters. Using the monthly potential temperature and salinity data of ORAS4, we calculated the monthly MLD as the depth at which the density changes by a threshold of  $0.05 \text{ kg m}^{-3}$  for depth of 5 m. The monthly MLD is interpolated to daily to estimate the heat flux terms (Rodrigues et al., 2019).

$$Q_0 = Q_s + Q_b + Q_e + Q_h \quad (2)$$

$Q_0$  is the net surface heat flux ( $\text{W m}^{-2}$ ), which includes the latent heat flux  $Q_e$ , and the sensible heat flux  $Q_h$  released from the ocean mixed layer, the net solar radiation received  $Q_s$ , and the net longwave radiation released  $Q_b$ . Finally, the  $Res$  include the remaining unresolved process, such as vertical diffusion, and entrainment. The heat budget analysis is also verified with HYCOM ocean

170 current datasets. All the heat budget terms are calculated from 1994–2015 and averaged for the two  
171 study regions. Anomalies are derived from the 1994–2015 daily climatology. Then we estimate the  
172 heat budget terms for the five days before the start date of MHWs in the selected regions.

173

### 174 **3. Results**

175 To investigate the changes in MHWs in the Indian Ocean, we first select those regions in the tropical  
176 Indian Ocean that experienced an increasing trend in MHWs during 1982–2018. The result section is  
177 organized into five sections. Section 3.1 describes the MHWs in the Indian Ocean and their trend. In  
178 section 3.2, we describe the seasonal climatology of MHWs for the regions where the trends are the  
179 largest. Section 3.3 addresses the role of dominant modes of climate variability on the MHWs in the  
180 tropical Indian Ocean. In section 3.4, we focus on the genesis and evolution of MHWs during the  
181 southwest monsoon season (June–September) and then describes the interaction between MHWs and  
182 the monsoon rainfall in section 3.5.

183

#### 184 **3.1 Observed trends in marine heat waves in the Indian Ocean**

185 The climatological mean distribution of MHW frequency during 1982–2018 is shown in Figure 1a  
186 and b, indicating that MHWs are generally observed in the northern parts of north Indian Ocean. The  
187 trend in the annual MHW frequency from 1982–2018 over the Indian Ocean is shown in Figure 1c.  
188 The western Indian Ocean region (41°E–56°E, 8°S–8°N) shows the most prominent trend in MHWs,  
189 annually, though climatologically it was not a region with frequent MHWs. The western Indian  
190 Ocean region has an increasing trend of 1.2–1.5 MHW events per decade ( $p < 0.01$ ) at each grid point.  
191 The northern Arabian Sea also shows a similar increasing trend, though not well-defined.  
192 Meanwhile, in the eastern Indian Ocean and central equatorial Indian Ocean (80°E–110°E, 0°–20°S),  
193 the trend is about 0.4 MHW events per decade.



194           The boreal summer monsoon months (June–September) are immensely crucial for the Indian  
195   Ocean rim countries because the rainfall during this season supports the food, water, and energy  
196   security of this region (Beal et al., 2020; Wang et al., 2020). SST variability in the tropical Indian  
197   Ocean regulates the monsoon circulation and rainfall. Recognizing the importance of the SSTs  
198   during the northern summer monsoon months, we investigate the changes in MHWs during this  
199   season (June–September), for 1982–2018 (Figure 1d). Climatologically, during this season, MHWs  
200   generally occur in the northern parts of the north Indian Ocean (Figure 1b). During June–September,  
201   there are two regions where MHWs activities are rapidly increasing, in terms of the frequency and  
202   the area covered. One is in the western Indian Ocean region, where the annual trend in MHWs  
203   frequency is also maximum. The second one is in the northern Bay of Bengal (85°E–93°E, 15°N–  
204   23°N) region, where a well-defined trend in MHW frequency is observed, at its maximum during the  
205   summer monsoon season (Figure 1d). These two regions are experiencing an increasing trend of 0.5  
206   events per decade during June–September. Apart from these two locations, the northeastern Arabian  
207   Sea also shows a similar increasing trend.

208           We further examined the month-wise trend of the frequency of MHWs over western Indian  
209   Ocean and northern Bay of Bengal region. For the western Indian Ocean region (in Figure 1e), we  
210   find that the increasing trend of MHW frequency is present in all months. The trend is most  
211   considerable in August to December, with the maximum in November. For the north Bay of Bengal  
212   region, the MHWs frequency trends are small in January to April and large in May to August, and  
213   moderate in September to December (Figure 1f). Hence, the western Indian Ocean region is crucial  
214   in the tropical Indian Ocean, experiencing a significant increasing trend in the frequency of MHWs  
215   year-round, while the north Bay of Bengal region is experiencing a significant trend during summer  
216   monsoon months.

217           Henceforth, we focus our analysis on the western Indian Ocean (41°E–56°E, 8°S–8°N) and  
218   north Bay of Bengal (85°E–93°E, 15°N–23°N) regions, where the MHW trends are the largest. We

219 identified individual MHW events based on the spatial mean SST time series over western Indian  
220 Ocean and north Bay of Bengal boxes in Figure 1d. There are 66 MHW events that occurred in the  
221 western Indian Ocean region during the 1982–2018 period, in which 21 events occurred during June–  
222 September. The north Bay of Bengal region witnessed 94 MHW events, and 34 out of these occurred  
223 during June–September. The time series of the annual and monsoon MHW frequency for western  
224 Indian Ocean and north Bay of Bengal are shown in Figure 1g, h. There is a significant rise in annual  
225 MHW frequency during 1982–2018 at a rate of 0.14 events per year for the western Indian Ocean  
226 and 0.09 events per year for the north Bay of Bengal. On the other hand, the MHW frequency during  
227 the monsoon season is increasing at a rate of 0.04 events per year in the western Indian Ocean region  
228 and 0.05 events per year in the north Bay of Bengal (Figure 1 g, h). It is evident from the time series  
229 that the trend of MHW frequency in the north Bay of Bengal during June–September shows higher  
230 values compared to the western Indian Ocean region during the same period.

231

### 232 **3.2 Seasonal climatology of marine heatwaves in the tropical Indian Ocean**

233 For the western Indian Ocean region, all the MHW metrics (except for the MHW events) show a  
234 double peak in the seasonal climatology signal during March and September months (Figure 2).  
235 During these two months, the duration of MHWs may reach 40 and 60 days, respectively. The mean  
236 intensity shows high seasonal variability. The mean intensity during March and September is highest  
237 with a mean value of 1.1°C. In the case of maximum intensity, it is 1.4°C during the peak months. In  
238 the case of area covered by the MHW events, it is 2 million km<sup>2</sup> during the peak months of March  
239 and September. Meanwhile, the number of MHW events show peaks during the May and October  
240 months.

241 For the north Bay of Bengal, the cumulative intensity and duration exhibit a peak during  
242 February, while the peak in the area, mean intensity, and maximum intensity is in May. Further, the  
243 number of events is maximum during May and October months (12 and 14 events respectively). The

seasonal signal of MHW metrics in the north Bay of Bengal shows peak values either in February or May. The cumulative intensity and duration in the peak month of February are 16°C days and 18°C days, respectively. The mean intensity during the May month is 1.1°C, while the maximum intensity is 1.3°C. During the peak month, the area is 0.45 million km<sup>2</sup>.

248

### 3.3 Role of Indian Ocean warming and dominant modes of climate variability on marine heatwaves

Recent research on MHWs (Laufkötter, et al., 2020, Holbrook et al., 2019, Frölicher et al., 2018) and the IPCC SROCC point out that MHW events are a manifestation of the global warming trend (Collins et al., 2019). A pattern correlation between the tropical SST trends and tropical MHW trends shows a significantly high correlation ( $r=0.8$  for annual values and  $r=0.6$  for boreal summer season) supporting this argument. Besides the global SST rise, various modes of climate variability favor MHW events by generating the necessary background conditions (Holbrook et al., 2019).

This section investigates the role of different climate modes on the occurrences of MHW events, particularly the association with El Niño, Indian Ocean basin-wide warming mode (IOB, Indo-Pacific warming generally occurring during the post- El Niño periods), Indian Ocean Dipole (IOD), and the North Atlantic Oscillation (NAO). Figure 3 shows the number of MHW days coincident with these climate modes or overlapping modes. An active phase of a climate mode is defined when the corresponding climate indices have a value larger than its long-term standard deviation. The absence of any climate modes during the MHW is indicated as “Nil”. It is important to note that the metric ‘MHW days’ is used instead of ‘MHW events’ for investigating the association between the MHWs and different climate modes. This is because a greater number of MHW events in a season or year does not necessarily mean a correspondingly greater number of MHW days, as there may be a greater number of short MHW events in some years with short

268 duration, and vice-versa. Regardless, we obtain similar results while using the metric ‘MHW events’  
269 also (Figure S1).

270 Correlation and composite analysis of the yearly count of MHW days in the western Indian  
271 Ocean region with the annual mean SSTs show that these events are associated with the El Niño,  
272 IOB (Indian Ocean warming), and negative North Atlantic Oscillation (NAO) (Figure 3a, b). Out of  
273 all the western Indian Ocean MHW days, the most significant number of MHW days occur under the  
274 Indian Ocean warming condition (Figure 3a, b). There are a significant number of MHW days when  
275 no climate modes are present. Regardless, there are a large number of MHW days under the positive  
276 IOD and negative NAO conditions. The spatial correlation between the MHW days in the western  
277 Indian Ocean region and mean SSTs for June–September shows significant associations with warm  
278 SSTs in the western Indian Ocean and El Niño and IOD. Most of the MHW days in June–September  
279 occurs without any influence of climate modes (Figure 3d).

280 Similar to the western Indian Ocean region, correlation and composite analysis of the yearly  
281 count of MHWs days in the north Bay of Bengal with the annual mean SST shows an association  
282 with the Indian Ocean warming, El Niño, and negative NAO (Figure 3e, f). Out of all the north Bay  
283 of Bengal MHW days, significant MHW days occur under the Indian Ocean warming condition.  
284 There are several MHW days associated with the negative NAO conditions following the IOB  
285 condition. Meanwhile, for June to September, the MHW days in the north Bay of Bengal appear to  
286 occur with warming in the north Indian Ocean (Figure 3g) and negative NAO pattern (Figure 3h).

287 In summary, occurrences of western Indian Ocean and north Bay of Bengal MHWs are more  
288 frequent while Indian Ocean warming is prominent basin wide (IOB) or when the western (for  
289 western Indian Ocean MHWs in summer) or northern (for Bay of Bengal MHWs in summer)  
290 exhibits warming. The western Indian Ocean SSTs also respond to the El Niño due to the subsidence  
291 of Walker circulation over these regions (Roxy et al. 2014, Xie et al., 2016). This subsidence inhibits  
292 deep convection and thereby suppresses the release of heat from the ocean to the atmosphere. Thus,

the Indian Ocean attains its maximum temperatures under the IOB mode. That is, the background warming in the Indian Ocean has a strong influence on the MHWs in the Indian Ocean basin on an annual timescale. During a positive IOD event, the western Indian Ocean becomes warmer than its climatology (Murtugudde and Busalacchi, 1999; Saji et al., 1999). June–September MHWs in the western Indian Ocean region are often associated with these positive IODs (Holbrook et al., 2019). The negative NAO phases are also associated with MHWs over the north Bay of Bengal region. Holbrook et al. (2019) and Mishra et al. (2012) show an association between negative NAO and north Indian Ocean warming. However, the mechanism between the negative NAO and north Indian Ocean SSTs needed to be explored in detail. Though the occurrences of MHWs in the Indian Ocean exhibit potential association with the climate modes described here, we do not investigate the mechanisms through which their causal relationships are manifested.

304

### 3.4 Local ocean-atmospheric interaction leading to the genesis and evolution of MHW events

In this section we explore the role of local ocean-atmospheric conditions leading to the initiation and the persistence of MHWs in the Indian Ocean. It is observed that for the western Indian Ocean MHWs, the downward solar radiation leads the SST peak by ~10 days. However, this lead-lag relation is weak ( $r = 0.13$ ). The increased downward solar radiation due to clear sky conditions may increase SST in the western Indian Ocean region but is not the primary reason for MHW genesis. Meanwhile, the reduced wind speed and evaporation (denoted by the negative wind anomaly and reduced upward latent heat flux anomaly in Figure 4b) leads the SST anomalies by ~3 days ( $r = -0.24$ ,  $p < 0.05$ ), assisting the MHW formation. Besides the air-sea fluxes, reduced wind speed also impacts the ocean current over the western Indian Ocean Region. The ocean currents in the western Indian Ocean region (driven by strong cross-equatorial monsoon winds) are usually strong and transport heat away from the equator. Hence, a weakening of the cross-equatorial winds can

317 potentially reduce ocean heat transport by accumulating the heat in this region, enhancing the  
318 MHWs.

319 To comprehend the spatial distribution of the lead-lag relationship, composites of different  
320 variables from a week before and after the MHW genesis date are presented in Figure 4b. The SST  
321 anomalies show a dipole pattern with cold anomalies at 15°N and warm anomalies at the equator  
322 prior to the genesis of western Indian Ocean MHWs. In Figure 4a, the region of cold SST anomalies  
323 can be observed north of the western Indian Ocean region a week prior to the MHWs initiation. The  
324 warm SST anomalies near the equator gradually become prominent as the MHW initiates.  
325 Interestingly, the cold SST anomalies (up to -0.5° C) at the north of the western Indian Ocean region  
326 is maintained consistently from about a month (30 days) to almost a week (6 days) prior to the  
327 MHWs genesis. The meridional SST difference between the north (15°N) and western Indian Ocean  
328 region is also maintained during the same period prior to the genesis of MHWs (supplementary  
329 information Figure S4c, d). These cold SST anomalies at 15°N and the meridional SST difference  
330 may have a significant role in reducing the strength of cross-equatorial wind flow (Figure 4b and  
331 supplementary information S4). The reduced wind speed (up to -1 m/s during the pentad leading to  
332 the MHW onset) not only reduces the air-sea fluxes (reduce evaporation) (Figure 4b and  
333 supplementary information S4) but also affects the strength of ocean currents, leading to decreased  
334 heat transport from the equator towards the north. These factors contribute to the MHW formation in  
335 the particular region. One week prior to the MHWs genesis, the clear sky condition over the western  
336 Indian Ocean region due to the weak cross-equatorial flow and less evaporation increases downward  
337 solar radiation. The increase in downward solar radiation further increases the SST. Therefore, from  
338 the lead-lag time series and the spatial composites, we identify the role of reduced heat transport,  
339 decreased evaporation from the ocean surface, and increased downward short-wave radiation behind  
340 the MHWs genesis over the western Indian Ocean region. We find the release of upward sensible

341 heat flux and latent heat flux from the ocean after 3–5 days of the MHWs genesis reduce the ocean  
342 temperature and thereby the MHW intensity.

343 To explore the ocean dynamics involved in the genesis of MHWs over the western Indian  
344 Ocean region, we performed an oceanic mixed layer heat budget analysis (Figure 6 a, b, c). We  
345 calculated the composites of the heat budget terms for the five days before the onset of MHWs (5-  
346 day average). The heat budget analysis is carried out for the MHWs between 1994–2015, based on  
347 the availability of ocean potential temperature and salinity data. Figure 6a, b shows the role of the  
348 advection terms and the heat flux terms on the rate of change of SST in the western Indian Ocean  
349 region. In the advection term, the heat transport by the zonal ocean currents (the zonal advection  
350 term) is dominant compared to the meridional component.

351 In comparison to the advection term, the heat flux term is found to be contributing more to  
352 the temperature change. In the net heat flux term, the net solar radiation received in the mixed layer  
353 and the latent heat stored (due to less evaporation) in the mixed layer are the major contributors. The  
354 solar heating of the ocean surface and decreased evaporative cooling favors the genesis of MHWs in  
355 the western Indian Ocean region. The time-integrated heat budget terms in Figure 6c reveal the time  
356 evolution of different heat budget parameters.

357 In the north Bay of Bengal region, reduced wind speed anomalies and evaporation lead the  
358 MHWs genesis by ~2 days ( $r=-0.38$ ) (Figure 5a). Due to weakened wind speed, evaporative cooling  
359 over the ocean surface becomes less, and hence the SST increases. An increased OLR and downward  
360 solar radiation lead SST by ~4 days with  $r$  values 0.28 and 0.31, respectively. Hence, the reduced  
361 evaporative cooling and increased incoming solar insolation (clear sky conditions) jointly raise the  
362 SSTs over the north Bay of Bengal region leading to the MHWs. From the spatial composites in  
363 Figure 5b, the SST shows a rapid increase coinciding with the MHW genesis day. It is seen that the  
364 northeasterly winds establish in the north Bay of Bengal region 5 days before the onset of MHW and  
365 weaken the southwesterlies over the particular region. This reduced wind speed leads to a decrease in

366 evaporation at the ocean surface, in turn reducing the release of upward latent heat flux from the  
367 ocean. A negative latent heat flux anomaly in the north Bay of Bengal region is observed 5 days  
368 before the onset of MHWs, confirming these results. Moreover, there is an increased downward solar  
369 radiation and increased OLR one week before the genesis of MHWs, peaking on the starting day of  
370 MHWs. We can infer that the decreased upward latent heat flux due to the decreased wind speed and  
371 the clear sky condition (increased downward short-wave radiation) contribute to the MHW genesis in  
372 the north Bay of Bengal region. After 3 days of the MHW genesis, there is a release of sensible heat  
373 and upward longwave radiation from the ocean, reducing the ocean temperature and helping  
374 terminate MHWs events.

375         It is worth noting that (Figures 6d, e, f) in the northern Bay of Bengal, the temperature change  
376 is mainly attributed to the net heat flux, and there is less contribution from the heat advection term.  
377 The latent heat (due to decreased evaporation) and net solar radiation have a prominent role among  
378 the heat flux terms. Meanwhile, the role of advection is minimal here. In a nutshell, it can be inferred  
379 that the weak wind causes decreased evaporative cooling of the ocean, while the increased solar  
380 heating is also accompanying the temperature rise in this region. Figure 6f represents the time-  
381 integrated heat budget terms. It is evident that for the north Bay of Bengal region, the MHW duration  
382 is comparatively less than the western Indian Ocean region. In summary, the role of reduced wind  
383 speed and evaporation is more prominent in north Bay of Bengal MHWs, than the western Indian  
384 Ocean MHWs.

385         The lead-lag and heat budget analysis here using NCEP reanalysis are cross-validated using  
386 ERA5 reanalysis products in the supplementary information (Figure S2 & S3). In the lead-lag  
387 analysis the ERA5 and NCEP show similar results. The significant lead-lag correlations of both the  
388 dataset are similar, which supports the proposed lead-lag relation of SST and other atmospheric  
389 conditions, except the correlation with OLR. In case of heat budget analysis, the ERA5 (Figure S5)  
390 and the NCEP (Figure 6) show a similar conclusion, indicating that the downward solar radiation and



latent heat fluxes contribute largely to the peak in SST. However, there are some disagreements also. For example, in the WIO region, the ERA5 indicates that the temperature advection by ocean currents is a larger contributor than the net heat flux (Figure S5a&b). Also, for the both regions, the downward solar radiation and latent heat fluxes are large in the ERA5 (Figure S5) as compared to the NCEP (Figure 6) reanalysis. The differences in the heat flux terms contribution may be due to the nature of the reanalysis products.

### **3.5 Interaction of marine heatwaves with the Indian summer monsoon**

The analysis in this section is focused on the summer monsoon rainfall variations during the MHWs over both the western Indian Ocean and north Bay of Bengal regions. We analyzed the mean pattern of SST, vertical velocity (omega at 500 hPa), wind (at 850 hPa), OLR, and vertically integrated moisture flux and the rainfall. It is fascinating that the MHWs over the two regions have the opposite impacts on Indian summer monsoon rainfall.

The SST anomaly composite during western Indian Ocean MHWs shows a warming pattern in this region. The SST anomalies vary from 0.9°C–1.2°C (Figure 7a). Moreover, negative omega (vertical velocity) anomalies at 500 hPa and OLR confirm enhanced convective activity during MHW days over the western Indian Ocean MHW region. Higher SST triggers the ascending motion of air and convection (Figure 7c, Figure S6a). At the same time, the circulation pattern shows strong northeasterly wind anomalies, indicating that the mean southwesterly monsoon winds are weak during this time (Figure S6a). The anomalous Hadley circulation during western Indian Ocean MHW events shows increased convective activities over the equatorial Indian Ocean, while the descending branch occurs over the Indian subcontinent (Figure 7g). This indicates that the western Indian Ocean MHWs are conducive for inducing dry conditions over the Indian landmass. The vertically integrated moisture flux divergence analysis contributes a more precise picture, suggesting an anomalous moisture flux divergence over the Indian subcontinent, with the moisture transported away towards

416 the western Indian Ocean region (Figure 7e). The mean pattern of rainfall over Indian landmass  
417 agrees with the results, with reduced rainfall across most of the subcontinent where the monsoon  
418 westerlies are prominent (Figure 7i).

419 In Figure 7b, the higher SST anomalies in the north Bay of Bengal region are apparent during  
420 June–September MHWs. The positive omega anomalies at 500 hPa and the positive OLR values  
421 imply dry subsidence and absence of cloud cover (clear sky condition) in this region during strong  
422 MHW events (Figure 7d, Figure S6b). However, negative OLR anomalies (above  $-15 \text{ W m}^{-2}$ ) and  
423 negative omega anomalies at 500 hPa level over the western India and adjacent ocean region suggest  
424 enhanced convection and strong ascending motion in these regions. The vertically integrated  
425 moisture flux anomalies (Figure 7f) indicate a convergence of the wind in the same region where the  
426 OLR and omega anomalies are negative.

427 Figure 7h shows the mean meridional circulation averaged over the  $41^\circ\text{E}$ – $100^\circ\text{E}$  for the north  
428 Bay of Bengal region during the June–September MHW days for the period 1982–2018. Over the  
429 southern part of the Indian subcontinent ( $0$ – $15^\circ\text{N}$ ), there is increased convection during MHW days,  
430 supporting the previous results that show an increased convection in the vertical velocity over the  
431 region, while there is a suppressed convection at the  $20^\circ\text{N}$  due to the dry subsidence over north Bay  
432 of Bengal. We find an anomalous moisture flux convergence over the Indian landmass and  
433 anomalous moisture flux divergence over the north Bay of Bengal, which provides the cause for the  
434 observed rainfall pattern. The moisture transport from the warm north Bay of Bengal region by the  
435 anomalous easterly winds plays a crucial role in enhancing the rainfall over the south peninsular  
436 Indian subcontinent. There is a convergence of southwesterly monsoon winds and anomalous  
437 easterly winds from the Bay of Bengal at 850 hPa over the south-west Indian subcontinent (Figure  
438 S6b). The moisture convergence introduces the convective instability over this region. To  
439 summarize, there is a significant relationship between the MHWs in the northern Bay of Bengal and  
440 increased summer monsoon rainfall over southwest India.

441

### 442 **3.5 Conclusion**

443 Here we have conducted a detailed investigation of the trends and genesis of MHW events in the  
444 tropical Indian Ocean—and its interaction with the Indian summer monsoon. We find that the trend  
445 in annual frequency of MHWs is relatively higher in the western equatorial Indian Ocean (41°E–  
446 56°E, 8°S–8°N), which experienced 66 events during the 1982–2018 periods. We further studied the  
447 trend in MHW frequency during the Indian summer monsoon period (June–September) and find that  
448 the trend in MHWs is prominent in the western Indian Ocean and the north Bay of Bengal (85°E–  
449 93°E, 15°N–23°N). The north Bay of Bengal experienced 94 MHW events, wherein 34 events  
450 occurred from June to September, while in the western Indian Ocean region, it was 21 events.

451 We further investigate the climate modes driving the MHWs over these two regions. It is  
452 observed that the long-term persistence of MHWs in the western Indian Ocean region is associated  
453 with the background SST warming primarily identified with the Indian Ocean basin-wide warming  
454 (IOB) and also the El Niño, IOD, and NAO. Roxy et al. (2014) and Abish et al. (2018) show that the  
455 western Indian Ocean is warming at a rapid pace since the 1950s, largely in response to  
456 anthropogenic warming but manifested through an asymmetry in the ENSO impact—whereby El  
457 Niño events cause anomalous warming in the WIO and La Niña events fail to cool the WIO. They  
458 also found that the ENSO events are more intense in the recent decades and this result in a positive  
459 SST skewness. Han et al. (2010) identifies a change in the local Hadley and Walker circulation that  
460 affect the distribution of sea level and temperature in the in the Indian Ocean, with an increase in the  
461 WIO. Regardless, the role of mean SST rise in the WIO is obvious (Roxy et al., 2020). Figure S7  
462 shows an increase in the SST in the WIO after year 2000 (both for annual and June–September) in  
463 comparison with pre-2000 period, indicating the role of background warming on the increase in  
464 MHWs in the WIO. The background warming and the MHWs potentially decrease the summer

monsoon rainfall over the central and north east India post-2000, as observed by the rainfall difference between the two periods (Figure S7c).

For the north Bay of Bengal MHWs, the longer duration of these events is linked to the IOB, El Niño, and NAO. Earlier studies have pointed out that El Niño, IOD and IOB are major contributors to anomalous warm SST events in the tropical ocean (Holbrook et al., 2019). Notably, the SST trend due to global warming is manifested through the increased number of MHW events.

We investigated the seasonal climatology of MHW metrics in both the selected regions. For the western Indian Ocean region, it is found that all the MHWs metrics have a double peak in the seasonal climatology during March and September months. The highest number of western Indian Ocean MHWs events occur in October. For the north Bay of Bengal, all the metrics show high variability during February or May. The highest number of north Bay of Bengal MHWs events occur during May and October months (12 and 14 events, respectively). Interestingly, these two months (May and October) are when the cyclones are active in the Bay of Bengal. Warm SSTs set an ideal precondition for cyclones, and it is hence necessary to closely monitor the basin to understand how these MHWs are interacting with the cyclones.

Focusing on the factors influencing the genesis of MHWs events in the tropical Indian Ocean, the results here show that in the western Indian Ocean region, MHWs are formed due to a relaxation of winds prior to the event. This tranquility in the winds is making the SST rise through two ways—through a decrease in the evaporative cooling at the ocean surface, and through a weakened transport of the heat by ocean currents. Apart from this, increased solar heating of the ocean surface due to reduced cloud cover also helps the formation of a warm pool in the western Indian Ocean region. We find that solar insolation plays a major role in MHW genesis from ocean mixed layer heat budget analysis. The reduced upward latent heat flux and zonal heat advection are the other major contributors. Interestingly, we observe an occurrence of cold SST (north of the western Indian Ocean region) region 35~40 days prior to western Indian Ocean MHWs and a relatively low SST gradient.

490 This low SST gradient and cold pool may be the reason for the weakening of cross-equatorial flow.  
491 The genesis of MHWs in the Tasman Sea and China's marginal seas also had a similar role in ocean  
492 dynamics (Oliver et al., 2017, Yao et al., 2020).

493 For the north Bay of Bengal region, it is observed that the reduction in wind speed and  
494 thereby reduction in the release of latent heat is one of the major causes for MHW genesis. Along  
495 with this, the increased solar radiation at the ocean surface also plays a key role. However, unlike the  
496 western Indian Ocean region, the signature of heat advection behind the genesis of MHWs is absent  
497 in the case of the north Bay of Bengal. In this study, we find that the western Indian Ocean MHWs  
498 have a longer persistence time, and the process of genesis is also slower than the MHWs in the north  
499 Bay of Bengal.

500 The MHWs in the western Indian Ocean and the north Bay of Bengal have strong links to the  
501 observed variability of the Indian summer monsoon rainfall. We find that both the MHWs are  
502 associated with the drying conditions over the central Indian subcontinent. However, there is a  
503 significant increase in the rainfall over south peninsular India in response to the MHWs in the north  
504 Bay of Bengal. Climate model projections suggest further warming of the Indian Ocean in the future,  
505 which will very likely intensify the MHWs (Collins et al., 2019) and their impact on the monsoon  
506 rainfall. Since the frequency, intensity, and area of marine heatwaves are increasing, it is essential  
507 that we closely monitor and forecast these events in advance in order to mitigate their impacts.

508

## 509 **Acknowledgments**

510 The Optimum Interpolated Sea Surface Temperature (OISST) and the Outgoing Longwave Radiation  
511 (OLR) are available from National Oceanic and Atmospheric Administration (NOAA) (Reynolds et  
512 al., 2007). The daily wind, latent heat flux, sensible heat flux, upward longwave radiation, downward  
513 solar radiation, surface net longwave radiation, and surface net solar radiation are available from the  
514 National Center for Environmental Prediction/National Centers for Atmospheric Research

(NCEP/NCAR) reanalysis data (Kalnay et al., 1996). For the analysis of the rainfall variability over the India, we used daily rainfall available from the Indian Meteorological Department (Pai et al., 2014). The ocean current data is available from the Ocean Surface Current Analysis Real-time (OSCAR), provided by the Earth Space Research (Dohan and Maximenko, 2010). J.S.S. acknowledges the support of Dr. P. O. Nameer, Dean of College of Climate Change and Environmental Sciences (CCES) and Dr. M. Rajeevan, Secretary to the Ministry of Earth Sciences (MoES), for supporting her visit to the Indian Institute of Tropical Meteorology (IITM).

522

### 523 **Author contributions**

524 M.K.R. conceived the study and J.S.S. performed the analysis. J.S.S., M.K.R., and P.D. contributed  
525 to the interpretation of the results and drafting of the manuscript for publication. A.A. performed  
526 some of the preliminary analysis.

527

### 528 **References**

- 529 Abish, B., Cherchi, A. and Ratna, S.B., 2018. ENSO and the recent warming of the Indian Ocean.  
530 *Int. J. Climatol.*, 38(1), pp.203-214.
- 531 Balmaseda, M.A., Trenberth, K.E., Källén, E (2013), Distinctive climate signals in reanalysis of  
532 global ocean heat content, *Geophys. Res. Lett.*, 40, 1754–1759, doi:1002/grl.50382.
- 533 Beal, L.M., Vialard, J., Roxy, M.K., Li, J., Andres, M., Annamalai, H., Feng, M., Han, W., Hood, R.,  
534 Lee, T. and Lengaigne, M., 2020. A Road Map to IndOOS-2: Better Observations of the  
535 Rapidly Warming Indian Ocean. *Bull. Am. Meteorol. Soc.*, 101(11), pp.E1891-E1913.
- 536 Benthuisen, J.A., Tonin, H., Brinkman, R., Herzfeld, M., Steinberg, C (2016), Intrusive upwelling in  
537 the Central Great Barrier Reef, *J. Geophys. Res. Oceans*, 121, 8395–8416,  
538 doi:10.1002/2016JC012294.
- 539 Chen, K., Gawarkiewicz, G., Kwon, Y.O., and Zhang, W.G. (2015), The role of atmospheric forcing  
540 versus ocean advection during the extreme warming of the Northeast US continental shelf in  
541 2012, *J. Geophys. Res. Oceans*, 120(6), 4324-4339.
- 542 Collins M., M. Sutherland, L. Bouwer, S.-M. Cheong, T. Frölicher, H. Jacot Des Combes, M. Koll  
543 Roxy, I. Losada, K. McInnes, B. Ratter, E. Rivera-Arriaga, R.D. Susanto, D. Swingedouw,  
544 and L. Tibig, 2019: Extremes, Abrupt Changes and Managing Risk. In: IPCC Special Report  
545 on the Ocean and Cryosphere in a Changing Climate [H.-O. Pörtner, D.C. Roberts, V.

546 Masson-Delmotte, P. Zhai, M. Tignor, E. Poloczanska, K. Mintenbeck, A. Alegría, M.  
547 Nicolai, A. Okem, J. Petzold, B. Rama, N.M. Weyer (eds.)].

548 Darmaraki, S., Somot, S., Sevault, F., Nabat, P., Cabos Narvaez, W.D., Cavicchia, L., Djurdjevic, V.,  
549 Li, L., Sannino, G., Sein, D.V (2019), Future evolution of Marine Heatwaves in the  
550 Mediterranean Sea, *Clim. Dyn.*, 53, 1371–1392, doi:10.1007/s00382-019-04661-z.

551 Dohan, K., Maximenko, N (2010), Monitoring Ocean Currents with Satellite Sensors,  
552 *Oceanography*, 23, 94–103, doi:10.5670/oceanog.2010.08.

553 Edward, J.P., Mathews, G., Raj, K.D., Laju, R.L., Bharath, M.S., Arasamuthu, A., Kumar, P.D.,  
554 Bilgi, D.S. and Malleshappa, H., 2018. Coral mortality in the Gulf of Mannar, southeastern  
555 India, due to bleaching caused by elevated sea temperature in. *Curr. Sci.*, 114(9), p.1967.

556 Elzahaby, Y., Schaeffer, A (2019), Observational Insight Into the Subsurface Anomalies of Marine  
557 Heatwaves, *Front. Mar. Sci.*, 6, doi:10.3389/fmars.2019.00745.

558 Foltz, G.R., Grodsky, S.A., Carton, J.A. and McPhaden, M.J., 2003. Seasonal mixed layer heat  
559 budget of the tropical Atlantic Ocean. *J. Geophys. Res. Oceans*, 108(C5).

560 Frölicher, T.L (2019), Chapter 5 - Extreme climatic events in the ocean, in: Cisneros-Montemayor,  
561 A.M., Cheung, W.W.L., Ota, Y. (Eds.), Predicting Future Oceans, *Elsevier*, 53–60,  
562 doi:10.1016/B978-0-12-817945-1.00005-8.

563 Frölicher, T.L., Fischer, E.M., Gruber, N, (2018), Marine heatwaves under global warming, *Nature*,  
564 560, 360–364, doi:10.1038/s41586-018-0383-9.

565 Hersbach, H. and Dee, D.J.E.N., 2016. ERA5 reanalysis is in production. *ECMWF newsletter*,  
566 147(7), pp.5-6.

567 Hobday, A.J., Alexander, L.V., Perkins, S.E., Smale, D.A., Straub, S.C., Oliver, E.C.J., Benthuisen,  
568 J.A., Burrows, M.T., Donat, M.G., Feng, M., Holbrook, N.J., Moore, P.J., Scannell, H.A.,  
569 Sen Gupta, A., Wernberg, T (2016), A hierarchical approach to defining marine heatwaves,  
570 *Prog. Oceanogr.*, 141, 227–238, doi:10.1016/j.pocean.2015.12.014.

571 Holbrook, N.J., Scannell, H.A., Gupta, A.S., Benthuisen, J.A., Feng, M., Oliver, E.C.J., Alexander,  
572 L.V., Burrows, M.T., Donat, M.G., Hobday, A.J., Moore, P.J., Perkins-Kirkpatrick, S.E.,  
573 Smale, D.A., Straub, S.C., Wernberg, T (2019), A global assessment of marine heatwaves  
574 and their drivers, *Nat. Commun.*, 10, 1–13, doi:10.1038/s41467-019-10206-z.

575 IPCC, 2019: IPCC Special Report on the Ocean and Cryosphere in a Changing Climate [H.-O.  
576 Pörtner, D.C. Roberts, V. Masson-Delmotte, P. Zhai, M. Tignor, E. Poloczanska, K.  
577 Mintenbeck, A. Alegría, M. Nicolai, A. Okem, J. Petzold, B. Rama, N.M. Weyer (eds.)].

578 Jackson, J.M., Johnson, G.C., Dosser, H.V., Ross, T (2018), Warming From Recent Marine  
579 Heatwave Lingers in Deep British Columbia Fjord, *Geophys. Res. Lett.*, 45, 9757–9764,  
580 doi:10.1029/2018GL078971.

581 Joh, Y., Lorenzo, E.D (2017), Increasing Coupling Between NPGO and PDO Leads to Prolonged  
582 Marine Heatwaves in the Northeast Pacific, *Geophys. Res. Lett.*, 44, 11,663-11,671,  
583 doi:10.1002/2017GL075930.

584 Kalnay, E., Kanamitsu, M., Kistler, R., Collins, W., Deaven, D., Gandin, L., Iredell, M., Saha, S.,  
585 White, G., Woollen, J. and Zhu, Y., 1996. The NCEP/NCAR 40-year reanalysis project. *Bull.*  
586 *Amer. Meteor.*, 77(3), pp.437-472.

587 Krishnan, P., Roy, S.D., George, G., Srivastava, R.C., Anand, A., Murugesan, S., Kaliyamoorthy,  
588 M., Vikas, N., Soundararajan, R (2011), Elevated sea surface temperature during May 2010  
589 induces mass bleaching of corals in the Andaman, *Curr. Sci.*, 100, 111–117.

590 Laufkötter, C., Zscheischler, J. and Frölicher, T.L., 2020. High-impact marine heatwaves attributable  
591 to human-induced global warming. *Science*, 369(6511), pp.1621-1625.

592 Liebmann, B., & Smith, C. A. (1996). Description of a complete (interpolated) outgoing longwave  
593 radiation dataset. *Bull. Am. Meteorol. Soc.*, 77(6), 1275-1277.

594 Metzger, E.J., Smedstad, O.M., Thoppil, P.G., Hurlburt, H.E., Cummings, J.A., Wallcraft, A.J.,  
595 Zamudio, L., Franklin, D.S., Posey, P.G., Phelps, M.W. and Hogan, P.J., 2014. US Navy  
596 operational global ocean and Arctic ice prediction systems. *Oceanography*, 27(3), pp.32-43.

597 Mills, K.E., Pershing, A.J., Brown, C.J., Chen, Y., Chiang, F.-S., Holland, D.S., Lehutha, S., Nye,  
598 J.A., Sun, J.C., Thomas, A.C., Wahle, R.A (2013), Fisheries Management in a Changing  
599 Climate: Lessons from the 2012 Ocean Heat Wave in the Northwest Atlantic, *Oceanography*,  
600 26, 191–195.

601 Mishra, V., Smoliak, B.V., Lettenmaier, D.P. and Wallace, J.M., 2012. A prominent pattern of year-  
602 to-year variability in Indian Summer Monsoon Rainfall. *Proc. Natl. Acad. Sci. U.S.A.*,  
603 109(19), pp.7213-7217.

604 Murtugudde, R., and Busalacchi, A. J. (1999). Interannual variability of the dynamics and  
605 thermodynamics of the tropical Indian Ocean. *Journal of Climate*, 12(8), 2300-2326.

606 Oliver, E.C., Benthuisen, J.A., Bindoff, N.L., Hobday, A.J., Holbrook, N.J., Mundy, C.N., and  
607 Perkins-Kirkpatrick, S.E (2017), The unprecedented 2015/16 Tasman Sea marine heatwave,  
608 *Nat.Comm.*, 8(1), 1-12.

609 Oliver, E.C., Burrows, M.T., Donat, M.G., Sen Gupta, A., Alexander, L.V., Perkins-Kirkpatrick,  
610 S.E., Benthuisen, J., Hobday, A.J., Holbrook, N.J., Moore, P.J. and Thomsen, M.S., 2019.  
611 Projected marine heatwaves in the 21st century and the potential for ecological impact. *Front.*  
612 *Mar. Sci.* 6, p.734.

613 Oliver, E.C.J., Donat, M.G., Burrows, M.T., Moore, P.J., Smale, D.A., Alexander, L.V., Benthuisen,  
614 J.A., Feng, M., Gupta, A.S., Hobday, A.J., Holbrook, N.J., Perkins-Kirkpatrick, S.E.,  
615 Scannell, H.A., Straub, S.C., Wernberg, T. 2018a , Longer and more frequent marine  
616 heatwaves over the past century, *Nat. Commun.*, 9, 1–12, doi: 10.1038/s41467-018-03732-9.

617 Pai, D.S., Sridhar, L., Rajeevan, M., Sreejith, O.P., Satbhai, N.S. and Mukhopadhyay, B., 2014.  
618 Development of a new high spatial resolution (0.25× 0.25) long period (1901–2010) daily  
619 gridded rainfall data set over India and its comparison with existing data sets over the region.  
620 *Mausam*, 65(1), pp.1-18.

621 Piatt, J.F., Parrish, J.K., Renner, H.M., Schoen, S.K., Jones, T.T., Arimitsu, M.L., Kuletz, K.J.,  
622 Bodenstein, B., García-Reyes, M., Duerr, R.S., Corcoran, R.M., Kaler, R.S.A., McChesney,  
623 G.J., Golightly, R.T., Coletti, H.A., Suryan, R.M., Burgess, H.K., Lindsey, J., Lindquist, K.,



624 Warzybok, P.M., Jahncke, J., Roletto, J., Sydeman, W.J (2020), Extreme mortality and  
625 reproductive failure of common murrelets resulting from the northeast Pacific marine heatwave  
626 of 2014-2016, *PLOS ONE* 15, e0226087, doi:10.1371/journal.pone.0226087.

627 Raj, K.D., Mathews, G., Bharath, M.S., Laju, R.L., Kumar, P.D., Arasamuthu, A. and Edward, J.P.,  
628 2018. Cushion star (*Culcitasthmideliana*) preys on coral polyps in Gulf of Mannar, Southeast  
629 India. *Mar Freshw Behav Physiol*, 51(2), pp.125-129.

630 Rodrigues, R.R., Taschetto, A.S., Gupta, A.S., Foltz, G.R (2019), Common cause for severe droughts  
631 in South America and marine heatwaves in the South Atlantic, *Nat. Geosci.*, 12, 620–626,  
632 doi:10.1038/s41561-019-0393-8.

633 Roxy, M.K., Modi, A., Murtugudde, R., Valsala, V., Panickal, S., Prasanna Kumar, S.,  
634 Ravichandran, M., Vichi, M. and Lévy, M., 2016. A reduction in marine primary productivity  
635 driven by rapid warming over the tropical Indian Ocean. *Geophys. Res. Lett.*, 43(2), pp.826-  
636 833.

637 Roxy, M.K., Ritika, K., Terray, P., Masson, S (2014), The Curious Case of Indian Ocean Warming,  
638 *J. Clim.*, 27, 8501–8509, doi:10.1175/JCLI-D-14-00471.1.

639 Roxy, M.K., Ritika, K., Terray, P., Murtugudde, R., Ashok, K., Goswami, B.N (2015), Drying of  
640 Indian subcontinent by rapid Indian Ocean warming and a weakening land-sea thermal  
641 gradient, *Nat. Commun.*, 6, 1–10, doi:10.1038/ncomms8423.

642 Roxy, M. and Tanimoto, Y., 2012. Influence of sea surface temperature on the intraseasonal  
643 variability of the South China Sea summer monsoon. *Clim. Dyn.*, 39(5), pp.1209-1218.

644 Saji, N.H., Goswami, B.N., Vinayachandran, P.N. and Yamagata, T., 1999. A dipole mode in the  
645 tropical Indian Ocean. *Nature*, 401(6751), pp.360-363.

646 Schaeffer, A., Gramouille, A., Roughan, M., Mantovanelli, A (2017), Characterizing frontal eddies  
647 along the East Australian Current from HF radar observations, *J. Geophys. Res. Oceans*, 122,  
648 3964–3980, doi:10.1002/2016JC012171.

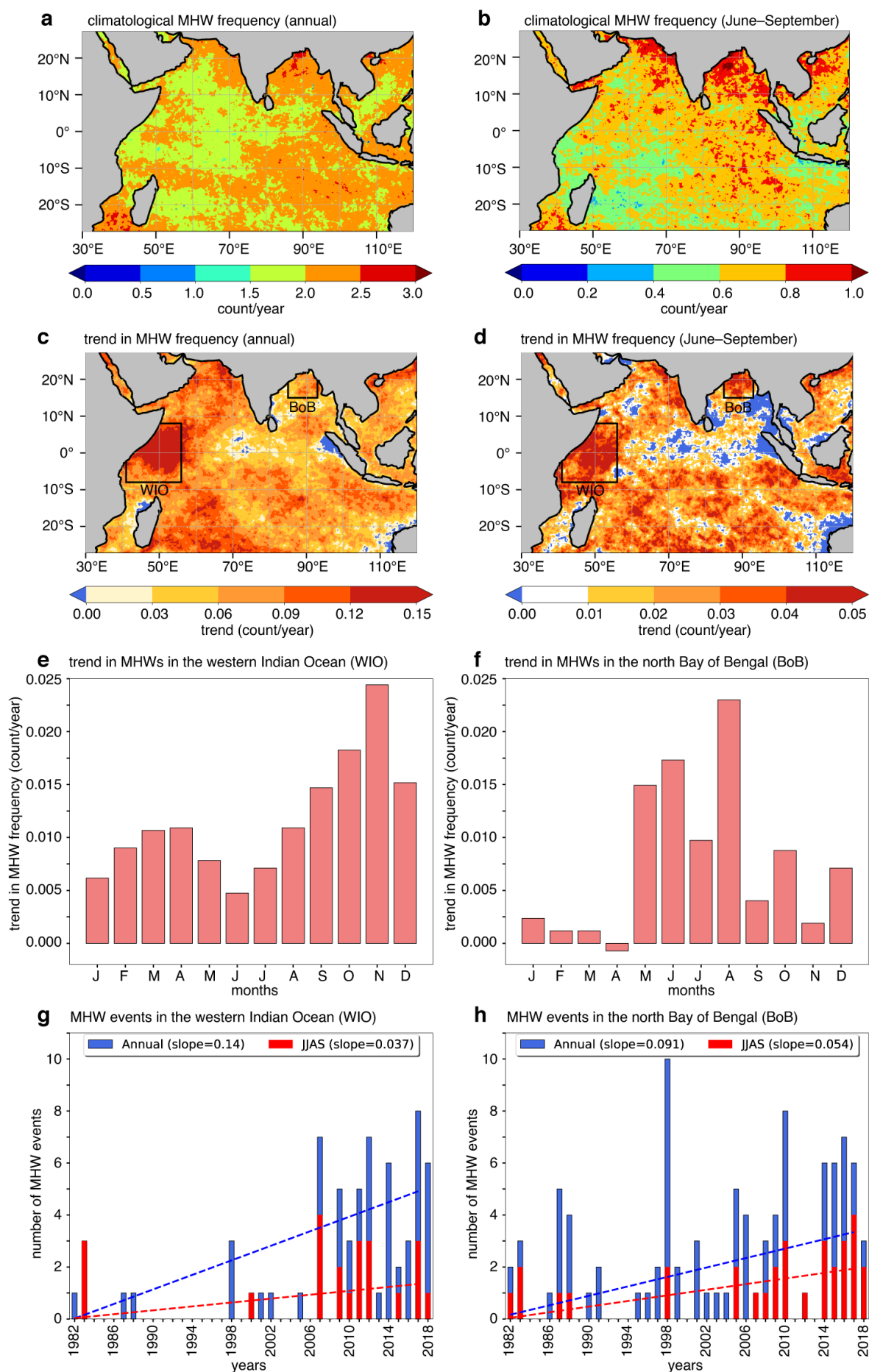
649 Schlegel, R.W., Oliver, E.C.J., Wernberg, T., Smit, A.J (2017), Nearshore and offshore co-  
650 occurrence of marine heatwaves and cold-spells, *Prog. Oceanogr.*, 151, 189–205,  
651 doi:10.1016/j.pocean.2017.01.004.

652 Singh, C. and Dasgupta, P., 2017. Unraveling the spatio-temporal structure of the atmospheric and  
653 oceanic intra-seasonal oscillations during the contrasting monsoon seasons. *Atmos. Res.*, 192,  
654 pp.48-57.

655 Walker, H.J., Hastings, P.A., Hyde, J.R., Lea, R.N., Snodgrass, O.E., Bellquist, L.F (2020), Unusual  
656 occurrences of fishes in the Southern California Current System during the warm water  
657 period of 2014–2018, *Estuar. Coast. Shelf Sci.*, 236, 106634,  
658 doi:10.1016/j.ecss.2020.106634.

659 Wang, B., Biasutti, M., Byrne, M.P., Castro, C., Chang, C.P., Cook, K., Fu, R., Grimm, A.M., Ha,  
660 K.J., Hendon, H. and Kitoh, A., 2020. Monsoons Climate Change Assessment. *Bull. Am.*  
661 *Meteorol. Soc.*

- 662 Xie, S.P., Kosaka, Y., Du, Y., Hu, K., Chowdary, J.S. and Huang, G., 2016. Indo-western Pacific  
663 ocean capacitor and coherent climate anomalies in post-ENSO summer: A review. *Adv.*  
664 *Atmos. Sci.*, 33(4), pp.411-432.
- 665 Yao, Y., Wang, J., Yin, J., Zou, X (2020), Marine Heatwaves in China's Marginal Seas and Adjacent  
666 Offshore Waters: Past, Present, and Future, *J. Geophys. Res. Oceans*, 125, e2019JC015801,  
667 doi:10.1029/2019JC015801.
- 668 Zhang, N., Feng, M., Hendon, H.H., Hobday, A.J., Zinke, J (2017), Opposite polarities of ENSO  
669 drive distinct patterns of coral bleaching potentials in the southeast Indian Ocean, *Sci. Rep.*, 7,  
670 doi:10.1038/s41598-017-02688-y.



672 **Figure 1: Climatology and** trend in MHW frequency (count/year) in the Indian Ocean during  
673 1982–2018 (a, c) annually and for (b, d) June–September, using NOAA OISST data. Month-  
674 wise trend of MHW frequency in the (e) western Indian Ocean (WIO, 41°E–56°E, 8°S–8°N)  
675 and (f) north Bay of Bengal (85°E–93°E, 15°N–23°N). Time series of the number of MHW  
676 days annually (blue bars), and during June–September (red bars), from 1982–2018 in (g) the  
677 western Indian Ocean and (h) the north Bay of Bengal region. Trend lines in the figure are  
678 statistically significant ( $p<0.05$ ).

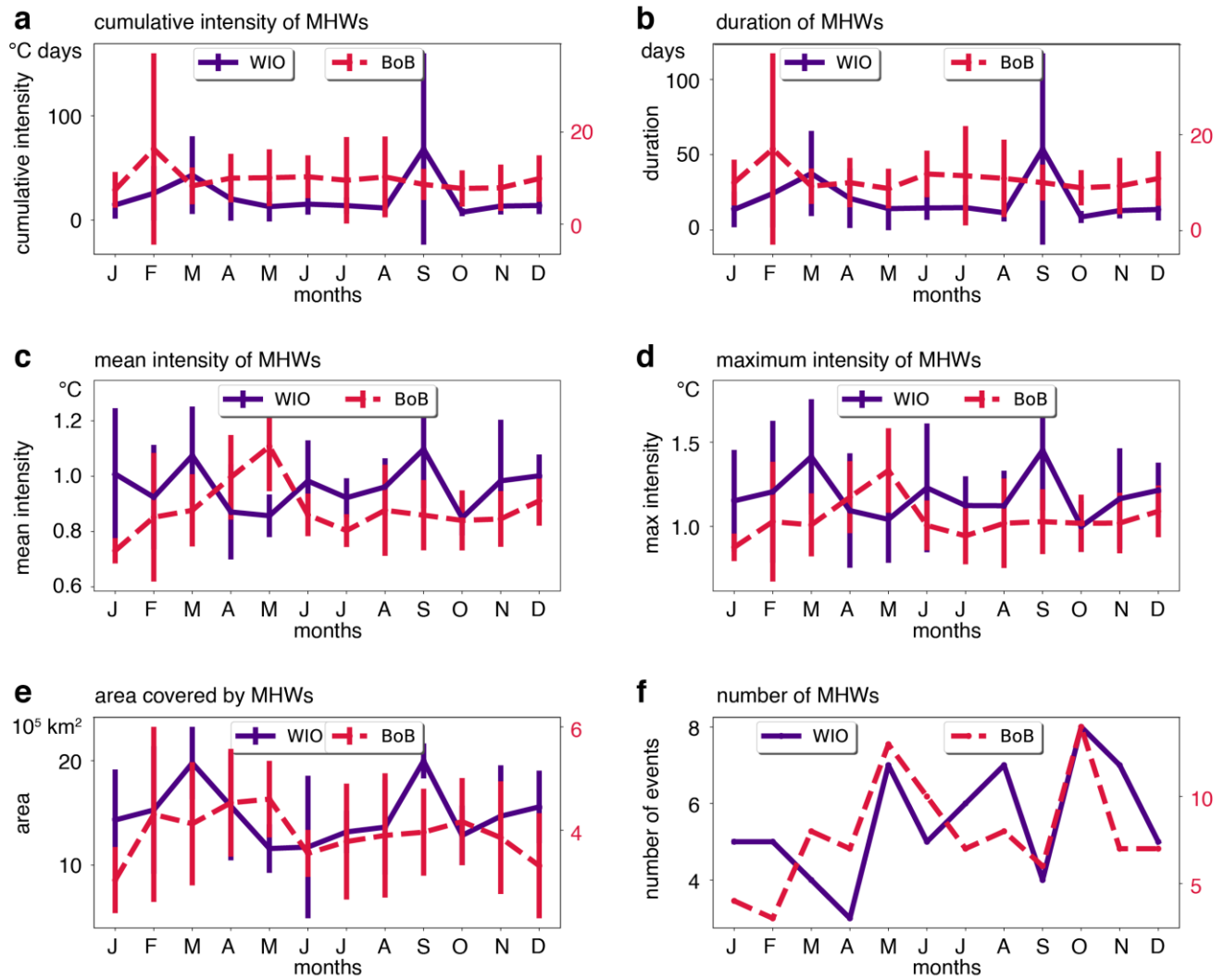
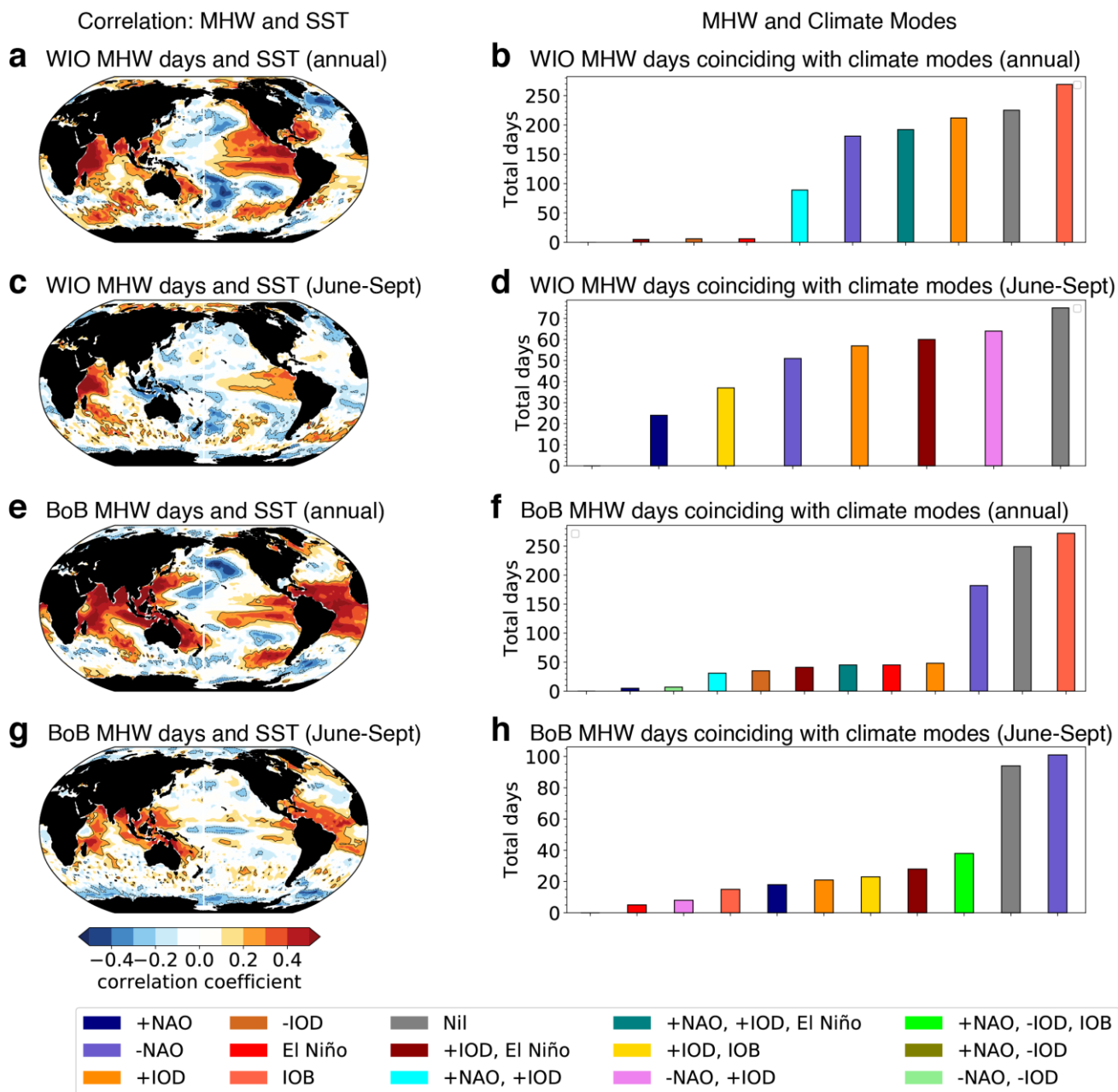
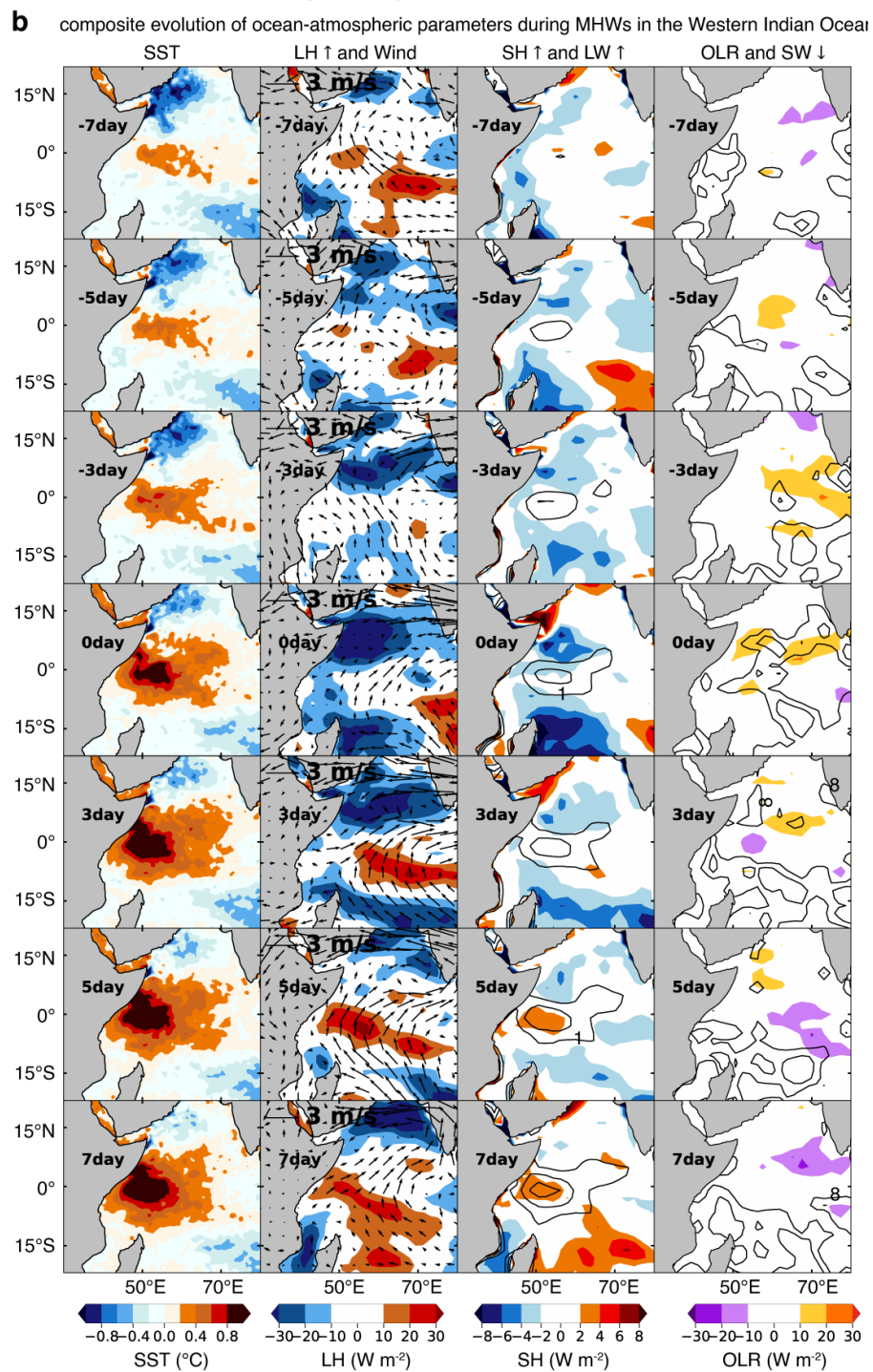
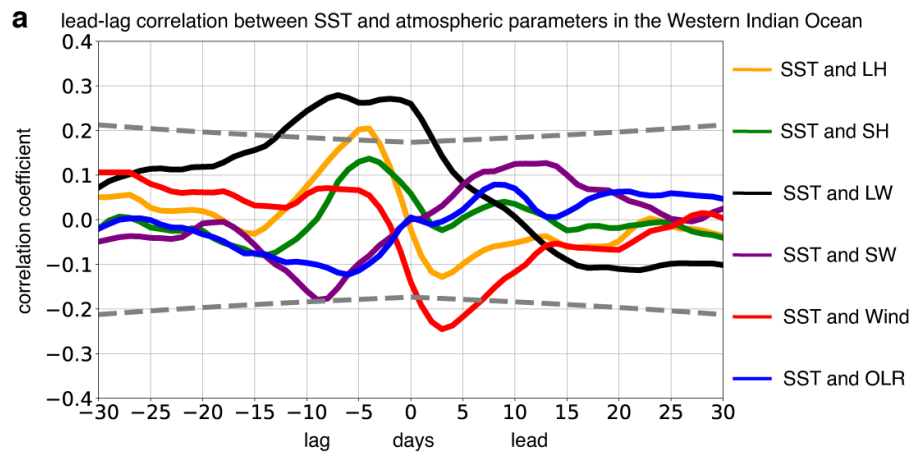


**Figure 2: Month-wise climatology of MHWs.** Month-wise distribution of (a) cumulative intensity ( $^{\circ}\text{C days}$ ), (b) mean intensity ( $^{\circ}\text{C}$ ), (c) duration (days), (d) maximum intensity ( $^{\circ}\text{C}$ ), (e) area ( $\text{km}^2$ ) and (f) the number of MHW events (month-wise sample size of MHWs, based on which the month-wise climatology is estimated), during 1982–2018 for the western Indian Ocean (WIO,  $41^{\circ}\text{E}$ – $56^{\circ}\text{E}$ ,  $8^{\circ}\text{S}$ – $8^{\circ}\text{N}$ ) and the north Bay of Bengal (BoB,  $85^{\circ}\text{E}$ – $93^{\circ}\text{E}$ ,  $15^{\circ}\text{S}$ – $23^{\circ}\text{N}$ ). The error bar represents the standard deviation.



686

687 **Figure 3:** Correlation between the total number of MHWs and global SST for (a, e) annual and (c, g)  
 688 June to September in the western Indian Ocean (WIO) and the north Bay of Bengal (BoB). The bar-  
 689 charts (b, d, f, h) indicate the total number of MHW days coinciding with climate modes. “Nil”  
 690 means the MHW days that do not coincide with any of the climate modes.



692 **Figure 4:** (a) The lead-lag correlation between SST and wind speed (red line), latent heat flux  
693 (orange line), sensible heat flux (green line), upward long wave radiation (black line), OLR (blue  
694 line) in the western Indian Ocean, estimated from the 30 days before and 30 days after the genesis of  
695 MHW events. The dotted lines represent the correlation significant at 95% confidence level.  
696 Composite evolution of (b) SST ( $^{\circ}\text{C}$ ), latent heat (LH,  $\text{W m}^{-2}$ ), wind ( $\text{m s}^{-1}$ ), OLR ( $\text{W m}^{-2}$ ), shortwave  
697 radiation (SW,  $\text{W m}^{-2}$ ), sensible heat (SH,  $\text{W m}^{-2}$ ), and longwave (LW,  $\text{W m}^{-2}$ ), in the western Indian  
698 Ocean before and during MHWs for the period 1982–2018, using NCEP/NCAR reanalysis datasets.  
699 Upward arrow represents the exchange of flux from ocean to atmosphere and downward arrow  
700 represents the exchange of flux from ocean to atmosphere.



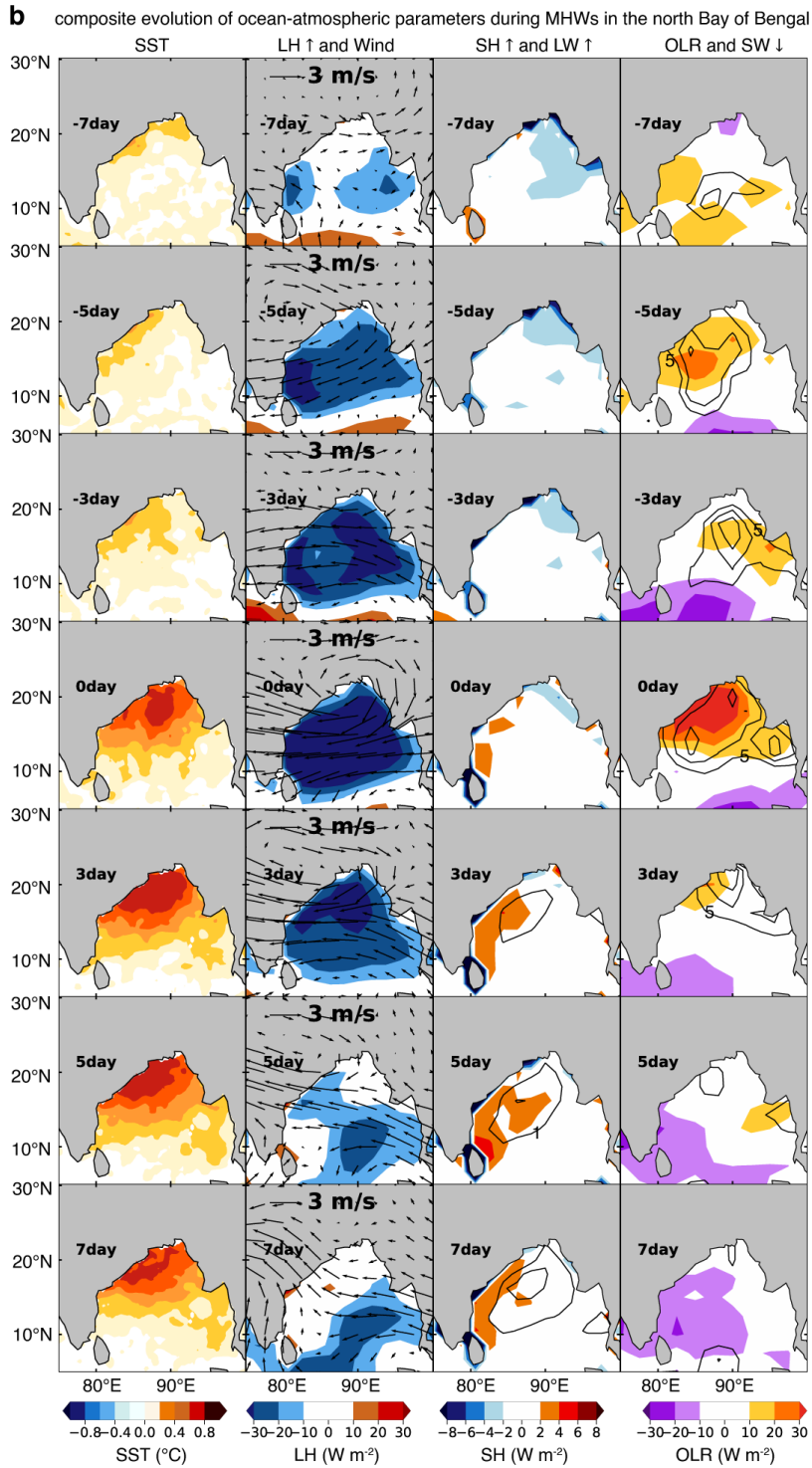
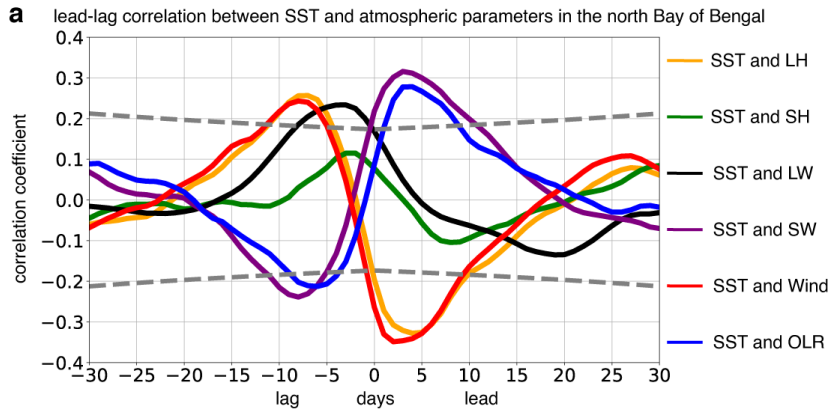


**Figure 5:** (a) The lead-lag correlation between SST and wind speed (red line), latent heat flux (orange line), sensible heat flux (green line), upward long wave radiation (black line), OLR (blue line) in the north Bay of Bengal, estimated from the 30 days before and 30 days after the genesis of MHW events. The dotted lines represent the correlation significant at 95% confidence level. Composite evolution of (b) SST ( $^{\circ}\text{C}$ ), latent heat (LH,  $\text{W m}^{-2}$ ), wind ( $\text{m s}^{-1}$ ), OLR ( $\text{W m}^{-2}$ ), shortwave radiation (SW,  $\text{W m}^{-2}$ ), sensible heat (SH,  $\text{W m}^{-2}$ ), and longwave (LW,  $\text{W m}^{-2}$ ), in the western Indian Ocean before and during MHWs for the period 1982–2018, using NCEP/NCAR reanalysis datasets. Upward arrow represents the exchange of flux from ocean to atmosphere and downward arrow represents the exchange of flux from ocean to atmosphere.

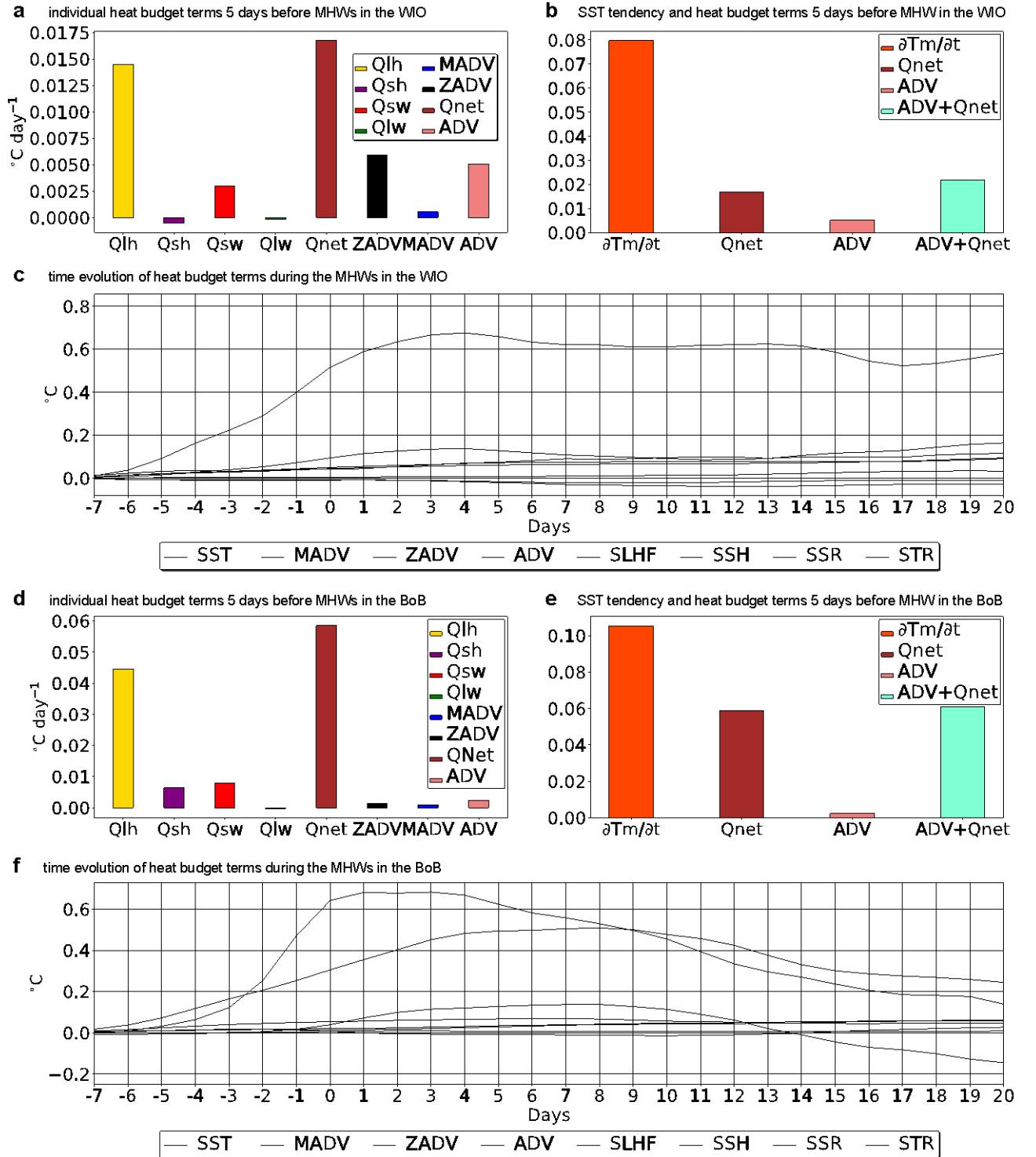
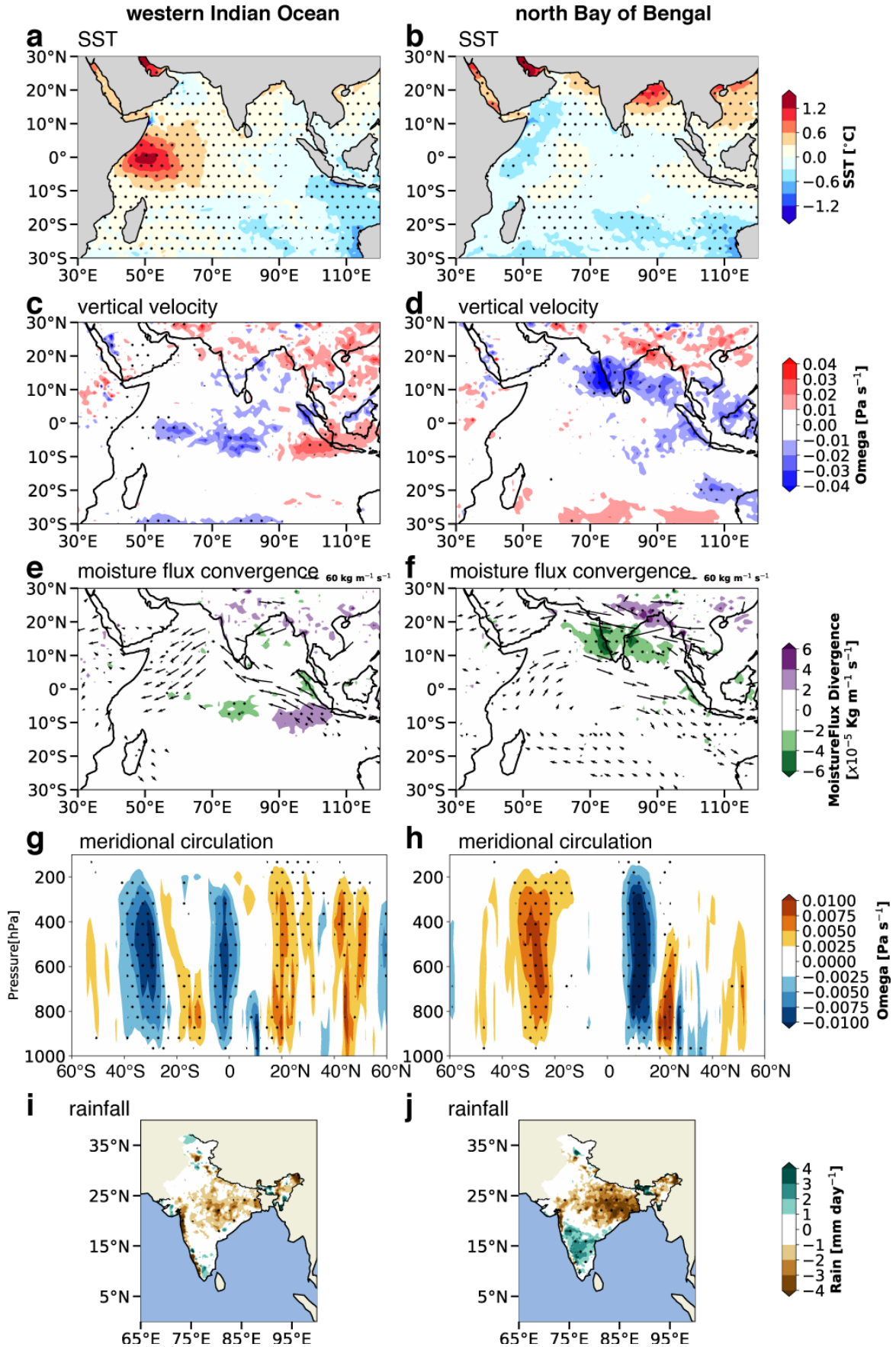


**Figure 6:** (a, d) Individual heat-budget terms (in  $^{\circ}\text{C day}^{-1}$ ) and (b, e) SST tendency with the heat budget terms 5 days before the genesis of MHW in the western Indian Ocean (WIO) and the north Bay of Bengal (BoB). (c, f) Time evolution of the heat budget terms (in  $^{\circ}\text{C}$ ) during the evolution of MHWs in the WIO and BoB. Heat budget terms estimated using the OSCAR current data and NCEP/NCAR fluxes during 1994–2015.

composite anomaly of ocean-atmospheric conditions during MHW events



718 **Figure 7:** Composite anomaly of daily (a, b) sea surface temperature anomalies (SST, °C ), (c, d)  
719 vertical velocity anomalies (omega at 500 hPa, Pa s<sup>-1</sup>), (e, f) moisture flux convergence (kg m<sup>-1</sup> s<sup>-1</sup>),  
720 (g, h) meridional circulation over 41°E–100°E (vertical velocity, Pa s<sup>-1</sup>) and (i, j) rainfall  
721 (mm day<sup>-1</sup>) during MHW days in the western Indian Ocean and north Bay of Bengal, during  
722 June–September, for 1982–2018. Stippling (black dots) indicates anomaly values significant at  
723 95% confidence level.

# Marine heatwaves in the Indian Ocean and their impact on the monsoon

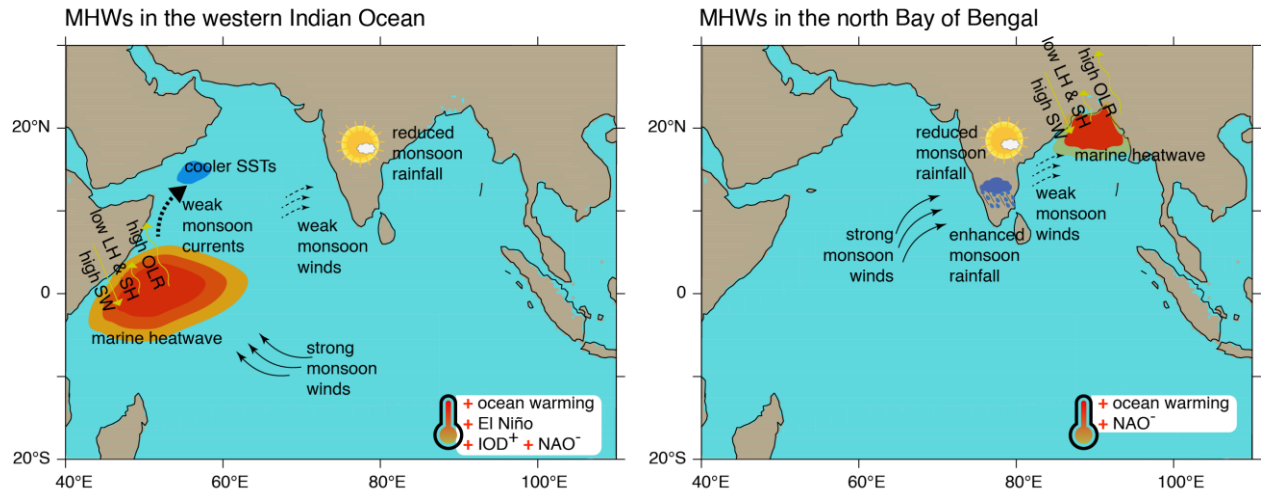


**Figure 8:** Schematic diagram depicting the factors leading to the genesis of MHW in (a) the western Indian Ocean and (b) the north Bay of Bengal, and its impact on the Indian summer monsoon rainfall. The legend alongside the thermometer indicates the association with ocean warming and various climate modes.